Numerical Investigation of Bleed on Three-Dimensional Turbulent Interactions Due to Sharp Fins

Datta Gaitonde* and Doyle Knight†
Rutgers University, Piscataway, New Jersey 08855

A numerical investigation is focused on the effect of bleed on the three-dimensional turbulent interaction generated by a sharp fin at Mach 3. For an incipiently separated configuration (8 deg fin, $Re_\delta = 5.6 \times 10^5$), 23% suction is applied over a rectangular area beneath the inviscid shock. Comparison with experimental data and analysis of computed results indicates that the effect of bleed is primarily to reduce surface angularity and upstream influence. The major portion of the flow is not influenced by suction. For a strong interaction (20-deg fin, $Re_\delta = 8.8 \times 10^5$), the effect of bleeding up to 25% of the boundary layer from two distinct regions on the plate jointly covering the region between the line of upstream influence and the base of the fin is studied. Numerical results are compared with available experimental data in the form of surface pressures and boundary-layer surveys of pitot pressure and yaw angle in the absence of bleed. The influence of suction on the overall flowfield and the previously observed vortical structure is remarkably modest, with significant effects restricted to the region adjacent to the plate near the bleed region.

I. Introduction

RESEARCH on three-dimensional shock wave-turbulent boundary-layer interactions ("three-dimensional turbulent interactions") finds utility in a number of high-speed aerodynamic applications such as aircraft components. A supersonic inlet flowfield, for example, is characterized by a pattern of oblique shocks, formed by the general curvilinear shape of the ramp and cowl surfaces, that interact with turbulent boundary layers on the walls. Dimensionless geometries such as the three-dimensional sharp fin configuration (SFC) are often employed to isolate the physics of such interactions from the geometrical complexity. The principal parameters for these flows are the Mach number (M_∞), the Reynolds number Re_δ based on the turbulent boundary layer thickness δ at the leading edge of the fin, the thermal boundary conditions, and the fin angle α.

Progress has been achieved in analyzing three-dimensional turbulent interactions with analytic,[1,2] experimental,[3-5] and numerical[6-8] techniques applied separately or in conjunction with each other. Numerical results for the sharp fin[7] (Fig. 1) and the swept compression corner[8,9] have shown good overall agreement with experimental measurements with modest local discrepancies in the prediction of upstream influence and skin friction values. Analysis of the computed flowfields confirms the principal flow feature—a large vortical structure aligned with the corner in agreement with the flowfield models of Token[10] and Kubota and Stollery.[4] A three-dimensional surface of separation (Fig. 2) emanates from the line of coalescence and spirals into the vortical center. A second surface, emanating from upstream, intersects the wall at the line of divergence and defines the extent of the fluid entrained into the vortical structure. Such a flowfield—specifically the large vortical structure and separated flow—is undesirable in applications such as aircraft inlets whose primary function is to provide a nearly uniform subsonic flow with high total pressure recovery at the compressor face.

The purpose of this paper is to examine a control method for the flowfield of interest. The need for boundary layer control studies has been recognized in the literature: "Despite the obvious importance of boundary layer control in high-speed air-breathing propulsion inlets, only two basic experimental studies of this problem involving swept interactions have been found in the literature both employing sharp fin shock generators."[11]

Several possible means of control may be proposed: 1) bleed, 2) blowing, 3) shock-shock interaction,[12] 4) modification of geometry,[13] and 5) vorticity modification of upstream flow. The focus of this paper is on the first of these options—the influence of bleed (suction) on three-dimensional turbulent interactions. Based on the availability of experimental data, the sharp fin geometry is selected for concreteness. The first set of computations is performed on an 8-deg fin geometry

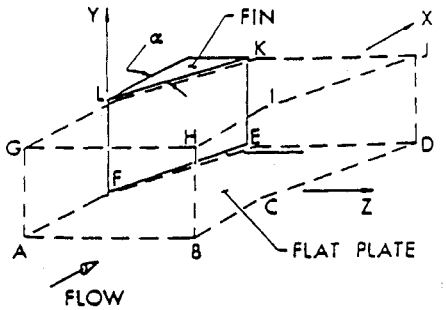

Fig. 1 Sharp fin configuration (SFC).

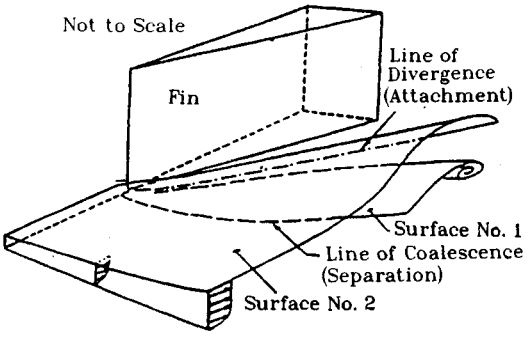

Fig. 2 Mean flowfield structure for SFC.

Received March 28, 1990; revision received July 31, 1990; accepted for publication Aug. 6, 1990.

*Graduate Student, Department of Mechanical and Aerospace Engineering; currently Visiting Scientist, WRDC/FIMM, Wright Patterson Air Force Base, OH 45433. Member AIAA.

†Professor, Department of Mechanical and Aerospace Engineering, P.O. Box 909. Associate Fellow AIAA.

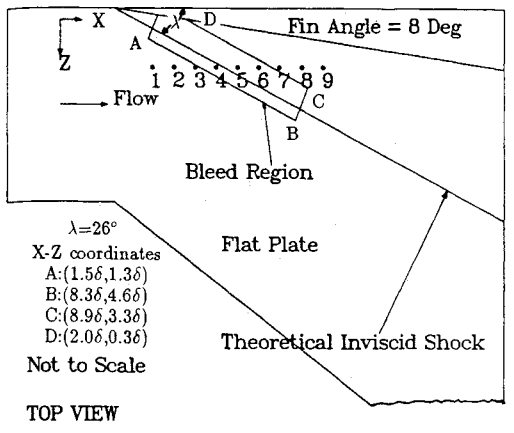

Fig. 3 Bleed region (8-deg SFC).

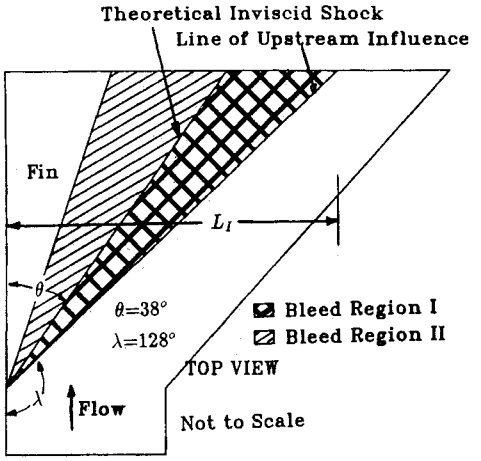

Fig. 4 Bleed regions (20-deg SFC).

with the bleed area and flow variables as exist in the experiments of Barnhart et al.[14] (Fig. 3). The configuration is incipiently separated in the absence of bleed. Although this study is not extensive enough to provide general guidelines, it serves at least to validate the algorithm and code utilized. The second set of computations is performed on a strong interaction (20-deg fin angle) with porous suction over two distinct regions (I and II) jointly spanning the entire area on the plate between the line of upstream influence and the base of the fin (Fig. 4). Several bleed rates are computed on this geometry as described below.

II. Governing Equations and Numerical Model

The governing equations are the full mean compressible Navier-Stokes equations using mass averaged variables and strong conservation form.[15] The molecular and turbulent Prandtl numbers are 0.73 and 0.9, respectively. Turbulence is modeled through the two-layer algebraic turbulent eddy viscosity model of Baldwin and Lomax[16] with the mixing length (l) as specified by the formula of Buleev.[17] The effect of bleed is incorporated through the bleed correction factor of Cebeci and Smith[18] as described in Ref. 19. This turbulence model has been validated for a variety of boundary-layer flows with zero, favorable, and adverse pressure gradients in the presence of suction.[20]

A three-dimensional transformation is employed as in Ref. 7 to facilitate the application of the numerical algorithm and the boundary conditions. The governing equations are solved with the hybrid explicit-implicit algorithm of Knight.[15] The code has previously been utilized successfully to predict turbulent interactions for the three-dimensional sharp fin,[7] swept compression corner,[8,9] and the double fin configuration.[19]

III. Classification of Computations

The x axis points in the general streamwise direction, y is plate normal, and z is the spanwise axis (Fig. 1). In each computation, a particular area (as below) is demarcated, and the mass flux at each grid point in the area is specified as a ratio of upstream freestream mass flux. The bleed parameter BP I defined as

$$\text{BP I} = \frac{\rho_w v_w}{\rho_\infty u_\infty} \tag{1}$$

is utilized to characterize the magnitude of suction where ρ is the density, u and v are the Cartesian components of the velocity in the streamwise and plate normal directions, and the subscripts w and ∞ indicate wall and freestream, respectively. The implementation corresponds to porous bleed as opposed to slot bleed. A more global characterization may be obtained by estimating the amount of incoming flow actually "seeing" the bleed region. This may be done in a simple manner by projecting the ray indicating start of suction on the upstream end of the domain. For example, for region I in Fig. 4, the boundary layer in distance L_I may be assumed to "see" the bleed region. BP II may be expressed as

$$\text{BP II} = \frac{\iint \rho_w v_w \, dA_b}{L \int_0^\delta (\rho u)_{\text{upstream}} \, dy} = \frac{\iint \rho_w v_w \, dA_b}{(\delta - \delta^*)\rho_\infty u_\infty L} \tag{2}$$

where δ is the boundary-layer thickness, δ^* is the displacement thickness, A_b is the area of bleed, and L is the appropriate upstream distance. The relevant flow and bleed parameters for all computations are provided in Tables 1 and 2.

Two fin angles are investigated:

8-Deg Sharp Fin Configuration

The recent experimental investigation by Barnhart et al.[14] on the effect of suction on supersonic flow past an 8-deg SFC

Table 1 Flow parameters[a]

Fin angle, deg	8	20
$\delta\|_{th}$, cm	3.1	1.3
$\delta\|_{ex}$, cm	3.11	1.40
$Re_{\delta\|th}$	5.6×10^5	8.8×10^5
$Re_{\delta\|ex}$	6.5×10^5	9.8×10^5
M_∞	2.95	2.95
P_t (kPa)	276	690
T_t (K)	300	251
T_w (K)	299	280

[a]Legend: δ = boundary-layer thickness, M = Mach number, P_t = total pressure, Re = Reynolds number, T_t = total temperature, T_w = wall temperature (fin and plate), subscripts th, ex = theoretical, experimental, and subscript ∞ = freestream.

Table 2 Classification of computations[a]

Case	A	B	C	D	E	F	G
Fin angle, deg	8	8	20	20	20	20	20
Bleed region	—	Fig. 3	—	I(Fig. 4)	II(Fig. 4)	I(Fig. 4)	I(Fig. 4)
BP I	0.000	0.040	0.000	0.010	0.010	0.025	0.050
BP II	0.00	0.23	0.00	0.05	0.08	0.13	0.25
CPU (h)	10.5	12.5	4.2	4.6	6.7	15.0	17.5
Flow time (T_c)	3.5	4.6	4.2	4.6	6.7	5.1	5.4

[a]Legend: BP = bleed parameter, T_c = characteristic time ($= L/U_\infty$).

is numerically investigated in this research. Two computations are performed on this geometry, no bleed (case A) and a case incorporating suction on the area displayed in Fig. 3 (case B) corresponding to a small region on either side of the theoretical inviscid shock footprint (TISF). The magnitude of suction is such that roughly 23% (= BP II) of the incoming boundary layer is ingested. The flow parameters and classification are summarized in Tables 1 and 2.

20-Deg Sharp Fin Configuration

Two distinct bleed regions are considered on the 20-deg SFC. Region I extends between the line of upstream influence and the TISF. Region II extends between the TISF and the fin base. All bleed and flow parameters are presented in Tables 1 and 2. Case C corresponds to flow past the 20-deg SFC without bleed. For case D, 5% (= BP II) bleed is applied on region I, whereas for case E the value of BP II is fixed at 8% on the area marked region II in Fig. 4. Further, cases F and G correspond to BP II = 13 and 25%, respectively, on region I. In this paper, only cases C, D, and E are discussed in detail. Further discussion of cases F and G may be found in Refs. 19 and 21.

IV. Computational Details

Nonuniform Cartesian grids are employed in all calculations. The three-dimensional grid is composed of a set of streamwise (x = const) planes concentrated in the bleed region for cases A and B and equally spaced with $\Delta x = \delta$ for cases C through G. Within each plane, two separate grid systems are employed—the "ordinary" and "sublayer" grid.[22] Eight grid points are utilized to resolve both fin and plate sublayers for cases A through E. For cases F and G, the plate sublayer resolution is increased to 12 points. The grid points adjacent to the plate and the fin are distributed using a combination of geometrically stretched and uniform spacings in the general fashion of Ref. 22. For cases A and B, a $40 \times 38 \times 54$ grid is utilized where the numbers refer to points in the streamwise, plate normal, and spanwise directions, respectively, including the sublayer mesh. Cases C, D, and E require $32 \times 38 \times 54$ grid points while for cases F and G, the increased plate sublayer resolution results in a $32 \times 42 \times 54$ mesh. Computations described in this paper were performed either on the 2-pipe VPS-32 machine at NASA Langley Research Center (cases A and B) or on the now decommissioned 4-pipe CYBER 205 at the NASA Ames Research Center (cases C through G). The CPU and corresponding flow development time required for each case are presented in the lower portion of Table 2.

Adequate resolution of different regions of the flow impose various constraints on permissible grid sizes. A complete set of criteria for judging the acceptability of a grid system does not exist at present, except perhaps for the process of successive grid refinement that is generally not feasible for three-dimensional Navier-Stokes calculations. The determination of the acceptability of a given grid system must be based on experience and previous computations.[15] The characteristics of the grids employed are detailed in Refs. 19 and 23 and, for each case, satisfy the constraints described in the literature in the average sense.[15] Previous computations with similar values have compared well with experiment.[15]

V. Boundary Conditions

The boundary conditions employed are described with reference to Fig. 1. The precise mapping from physical to computational domain is achieved with a computational grid. The upstream boundary ABHG is located 4.6 $\delta|_{th}$ upstream of the fin leading edge for cases A and B, 5.0 $\delta|_{th}$ for cases C through G. The incoming flow is assumed to be two-dimensional and is generated with a separate two-dimensional compressible boundary-layer code[20] utilizing the Baldwin-Lomax turbulent eddy viscosity model by matching the momentum thickness with available experimental values. Symmetry conditions are applied on the plane of symmetry upstream of fin leading edge (AFLG). On the fin surface (LFEK), the velocity vector and the normal pressure gradient are assumed zero, and a fixed surface temperature is specified as in Table 1. On the flat plate (ABCDEF), the components of the velocity vector are specified zero except where bleed is applied in the appropriate areas for cases B, D, E, F, and G by specifying the normal mass flux, $\rho_w v_w / \rho_\infty u_\infty$ (BP I in Table 2). The normal pressure gradient is assumed zero, and the surface temperature is fixed as for the fin surface (Table 1). The streamwise length of the physical domain is restricted so that the outgoing flow is supersonic except in a small portion of the boundary layer, and as such, the zero gradient extrapolation condition is applied at the downstream boundary (EKJD). For cases A and B, this boundary is located 17.8 $\delta|_{th}$ downstream of the fin leading edge whereas for cases C through G, the distance is 26 $\delta|_{th}$. The right boundary (BCDJIH) is assumed to be sufficiently far from the fin to ensure that the boundary layer is locally two-dimensional and therefore a simple gradient boundary condition $\partial/\partial_z = 0$ is employed. This requires that the shock wave pass out the downstream boundary (EKJD). Finally, the top boundary (HIJKLG) is located far enough—roughly 8 $\delta|_{th}$ for all cases—away from the corner formed by the plate and the fin to permit the assumption of two-dimensional flow in planes parallel to this boundary. A zero gradient boundary condition is therefore employed.

VI. Results

For the purpose of brevity, several results are presented without figures. A more detailed description of this work may be found in Ref. 21.

Suction on 8-Deg Sharp Fin Configuration

The geometrical configuration, bleed region, and other significant parameters of the two computations (cases A and B) on the 8-deg SFC are described in Fig. 3 and Tables 1 and 2. Results are first compared with experimental data and the flow is then examined with particle traces.

Comparison with Experiment

The experimental data utilized for comparison purposes were obtained at the NASA Lewis Research Center and are reported in Barnhart et al.[14] They utilize two Mach numbers, 2.48 and 2.95. The latter is relevant to this research and experimental results, published only in the presence of bleed, include surface (static pressures and wall flow angles) and boundary-layer measurements (pitot pressure and yaw angles). Each of these is compared below with computed results.

It is important to note one fundamental distinction between the computed and experimental configuration. In the experiment, suction is applied by perforations on the plate in conjunction with a vacuum boost pump downstream of the suction plenum. Since the surface pressure increases into the interaction, the experimental local bleed rate, which was not measured, is probably variable, increasing generally in the streamwise direction at any given spanwise location. For lack of precise information on local bleed variation on the plate, the computation assumes uniform bleed such that the total bleed mass rate over the entire bleed area matches experimental observation. It is expected, therefore, that computed bleed values exceed experimental values in the vicinity of the upstream end of the bleed domain. The reverse situation may be expected at the downstream end. In the following discussion, distances are normalized with the experimental upstream boundary-layer thickness ($\delta|_{ex} = 3.1$ cm). Further, the term "experimental data" is assumed to imply in the presence of bleed since no data are published in Ref. 14 without suction for this configuration. The strict comparison is therefore restricted to case B.

The computed (case B only) and experimental surface pressures at four spanwise locations ($Z = z/\delta$) are plotted in Fig. 5 vs relative location from the TISF [$(x - x_s)/\delta$]. The profiles at all locations collapse roughly on a single curve. Further,

while the upstream pressures up to $(x-x_s)/\delta \sim -4$ match well as expected, the computation displays significantly lower upstream influence. Experimental pressures begin to rise at $(x-x_s)/\delta \sim -1.5$ whereas the initial computed pressure rise occurs at $(x-x_s)/\delta \sim 0$, i.e., at the theoretical inviscid shock location. This discrepancy may be at least partly attributed to the assumption of uniform bleed in the computation. Since the effect of bleed is to lower upstream influence, a higher local computed bleed value (over experiment) may explain the results shown. The maximum deviation between computed and experimental results ($\sim 25\%$) occurs near the location of the inviscid shock. Near the center of the suction region, the computed and experimental values match as a result of more rapid computed pressure rise. The overall pressure rise at each spanwise location matches experiment and is only slightly lower (by $\sim 3\%$) than the theoretical pressure rise ($p_2/p_1 = 1.78$). A drop in surface pressure is evident at the onset of the bleed region for the $Z = 2.79$ and 3.44 locations, indicating a small local spanwise pressure oscillation. This is currently thought to be the result of high local bleed values at the individual grid point locations that lie precisely at these points.

The comparison with experimental surface yaw values at the same spanwise locations is displayed in Fig. 6. The value α/θ is plotted on the ordinate where α is the turning angle and θ is the fin angle. As anticipated upstream of the interaction, $(x-x_s)/\delta \sim -4$, yaw angles are roughly zero. Within the interaction, $-3<(x-x_s)/\delta<2$, experimental values display considerable scatter and indicate an earlier turning of the flow than does the computation. The discrepancy is again partly attributable to differences in local bleed rates. Computations predict lower turning angles at the upstream edge of the bleed region because local bleed values are higher than probably exist in the experiment. Both computation and experiment display maximum turning angles lower than the shock angle (corresponding to the value 3.23 in Fig. 6), although maximum experimental values exceed those computed by roughly 15%. Note that maximum turning occurs behind the inviscid shock. Further downstream, computed values display turning angles twice the fin angle, whereas experimental values approach the fin angle.

The location of the nine experimental boundary-layer surveys where pitot pressure and yaw angle profiles were measured is exhibited in Fig. 3. Figure 7a displays pitot pressure profiles at each of the nine stations. At station 1, upstream of the interaction, the experimental values (markers) match both the no-bleed (solid line) and bleed (dotted line) cases and resemble a two-dimensional profile similar to that existing at the upstream end of the domain. At station 2, the computed curves are generally similar to those at station 1, although in the region between $0.3<y/\delta<1$, experimental values are slightly lower. At the upstream edge of the bleed domain (station 3), both computed and experimental values in the presence of bleed display modestly lower values in the upper half of the boundary layer. At station 4, on the shock location, case A displays a small pitot pressure overshoot typical of compression fans (see, for example, Fig. 12 for the 20 deg interaction). The effect of bleed (case B) is to increase pitot pressure values up to about $y/\delta \sim 0.3$ compared to the no-bleed case, beyond which the values are lower. The experimental results agree with case B beyond $y/\delta>0.3$, although closer to the plate, more conformity is obtained with the no-bleed case. A similar crossover of no-bleed and bleed profiles is observed at station 5, which is the first station located downstream of the theoretical shock. Comparing case B with experiment, in the region $0<y/\delta<0.8$, the computed values overpredict pitot pressure values. The situation is reversed higher into the boundary layer. At stations 6, 7, 8, and 9, the profiles all display similar qualitative behavior. The "crossover" of bleed and no-bleed profiles occurs successively higher into the boundary layer. In general, experimental values agree with case B close to the plate, although higher into the boundary layer, experimental values match no-bleed results quite closely, indicating that the effect of bleed propagates higher into the boundary layer in the computation than in experiment.

The computed and experimental yaw angles are displayed in Fig. 7b. At station 1, upstream of the interaction, yaw angles are negligible throughout the boundary layer as anticipated. At station 2, the effect of bleed is to lower yaw angle values below the no-bleed values up to about $y/\delta \sim 0.5$. At the surface, computational values exceed experimental values. At station 3 located at the start of the bleed region, case A exhibits significant surface turning, whereas computed yaw angles for case B assume small values throughout the boundary layer in agreement with the previously observed reduction of upstream influence with suction. Experimental values lie between those for cases A and B. Downstream of the inviscid shock (station 5), the correspondence between case B and experiment is good, with the computations tending to slightly underpredict yaw angles. The effect of bleed is to reduce yaw angles in the boundary layer by as much as 50% at the surface. Further downstream, at station 6, although case B displays lower yaw angles, experimental values parallel case A more closely. At stations 7 and 8, located downstream of the bleed region, the effect of suction is more modest. The comparison between experiment and case B is very good at station 7. Experimental observations display lower turning at close

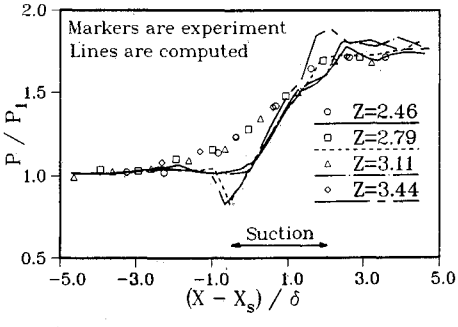

Fig. 5 Comparison of surface pressure (case B) with experiment (8-deg SFC).

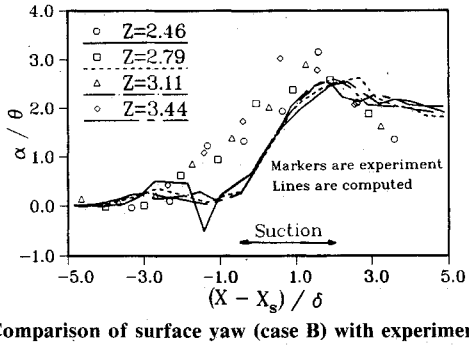

Fig. 6 Comparison of surface yaw (case B) with experiment (8-deg SFC).

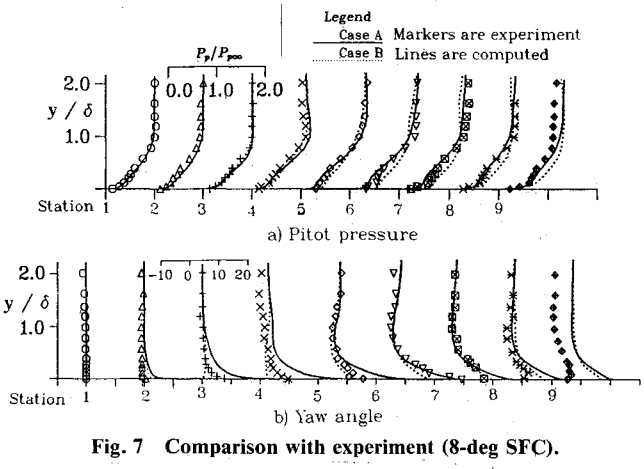

Fig. 7 Comparison with experiment (8-deg SFC).

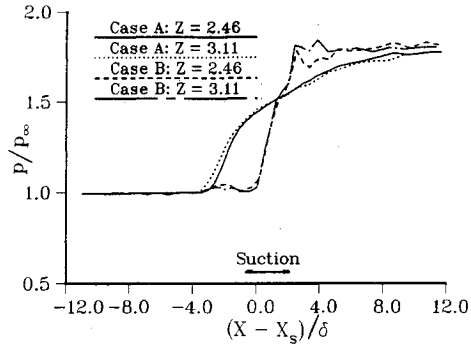

Fig. 8 Effect on surface pressure (computed) (8-deg SFC).

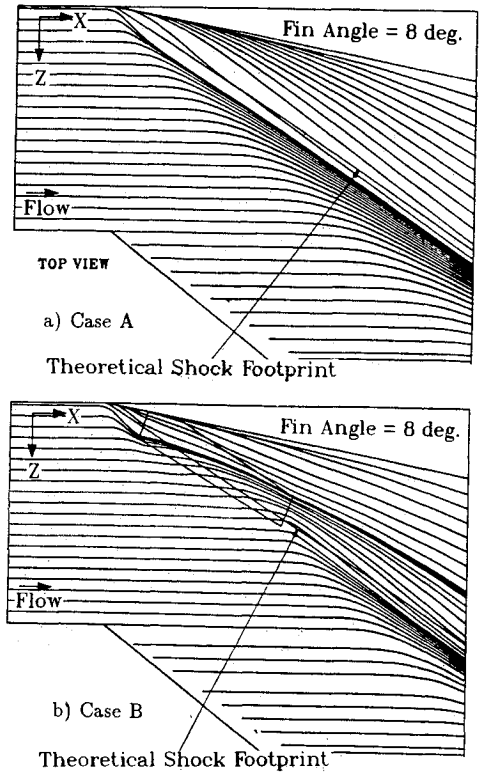

Fig. 9 Surface streamlines (8-deg SFC).

proximity to the plate at station 8. At station 9, located far downstream of the bleed region, the effect of bleed is restricted to the region $0 < y/\delta < 0.6$. Experimental values are significantly lower at this location and do not obtain the anticipated fin angle at large values of y/δ.

Analysis of Computed Flowfield

Figure 8 compares surface static pressure at two spanwise locations for cases A and B. For each case, the two profiles coalesce on one curve. While the total pressure rise is unaltered, upstream influence determined by initial pressure rise is reduced, and the rate of pressure rise in the interaction increases with bleed. Other important observations mentioned without accompanying figures (see Refs. 21 and 23) include 1) local skin friction values display steep increases in the bleed region and are not affected elsewhere; 2) bleed completely eliminates the upstream fan of the compression system near the plate, resulting in a somewhat tightened shock structure; 3) eddy viscosity values are observed to be lower in the boundary layer in the vicinity of the bleed region; and 4) no significant influence of bleed is observed on the flow variables in the essentially inviscid regions extending beyond $y/\delta \sim 2.5$.

The computed skin friction lines ("surface streamlines") are displayed in Fig. 9 for cases A and B, respectively. For case A, surface streamlines display maximum turning angles roughly equal to the shock angle. The flow may therefore be termed incipiently separated by Stanbrook's criterion.[3] No clear line of coalescence is visible, though the lines display bunching slightly upstream of the inviscid shock trace. For case B, significant reduction in surface angularity is observed in the bleed region only. Surface streamlines originating near the fin leading edge follow trajectories similar to those for case A. Upon reaching the bleed region, however, they straighten out and move parallel to the upstream flow for a short distance, gradually asymptoting the shock angle downstream of the bleed region. Several lines passing through the furthermost upstream end of the bleed region follow a single group of closely bunched lines passing out the downstream end of the bleed region.

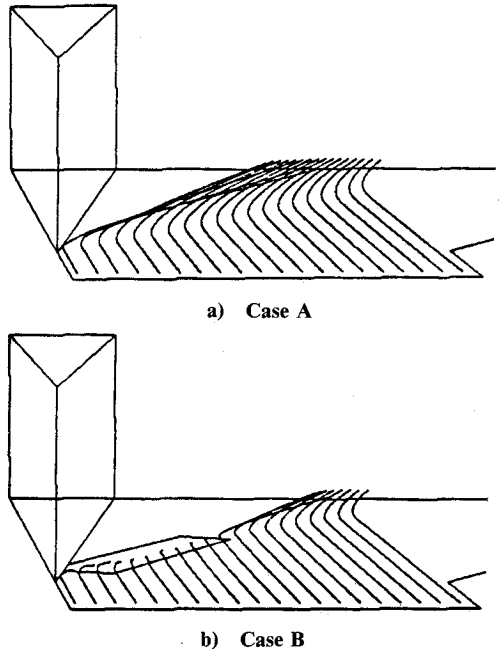

Fig. 10 Particle traces, $y/\delta = 0.1$ (8-deg SFC).

The flowfield was analyzed with exhaustive sets of traces of particles released at various heights above the plate at the upstream end of the domain. For brevity, only a few sets are discussed. Particles released within the sublayer ($y/\delta = 0.0001$) follow the general trajectory of the surface streamlines as anticipated for case A (not shown). In the presence of bleed, however, particles are ingested at the leading edge of the bleed region if released appropriately close to the fin. Particles at larger spanwise distances escape the influence of suction. A similar pattern is observed up to about $y/\delta = 0.01$. Further into the boundary layer, at $y/\delta = 0.1$ (Fig. 10), case A displays significant flow turning, although the clear vortical structure sketched in Fig. 2 and observed subsequently for the stronger interaction (see Fig. 16, for example) is not apparent. Several particles originating near the fin and whose no-bleed trajectory passes over the bleed region are ingested in case B roughly at the center of the bleed region. Particles released close to the plane of symmetry up to about 0.2δ from the plate are ingested at the trailing edge of the bleed region (not shown). Particles released at large spanwise distances are not affected. At $y/\delta = 0.3$ (not shown), none of the particles are ingested, although the traces are slightly altered by suction and display modestly lower yawing. At $y/\delta = 1$ (not shown), the effect of bleed is entirely negligible.

Suction on 20-Deg Sharp Fin Configuration

Computed results are first formally compared with available experimental data in the form of surface pressures, boundary-layer pitot pressure, and yaw angle profiles. Since

no bleed is imposed in these experiments, direct comparison with theory is limited to case C (no bleed). In the following discussion, the upstream boundary-layer thickness $\delta|_{th}$ is utilized to scale distances (cf., Ref. 24 for alternate scales). Streamwise distances x, unless otherwise mentioned, are measured relative to the location of the inviscid shock x_s at the relevant spanwise z position. Flow variables are normalized by their freestream values upstream of the interaction.

Effect of Suction on Flow Variables

The 14 experimental stations described in Knight et al.[7] are located in the general shape of a cross (Fig. 11) with stations 1 and 2 located upstream of the interaction, 3 and 13 at about the line of upstream influence, stations 4, 5, 6, and 12 in region I, while 7–11 and 14 lie in region II. The precise coordinates of these stations are provided in Ref. 7. Experimental and numerical results available in the form of pitot pressure and yaw angle boundary-layer surveys are compared at each of the above stations, although for the purpose of brevity only some plots (stations 5 and 8) are presented here.

At stations 1 and 2, located upstream of the interaction, the pitot pressure and yaw angle profiles (not shown—see Ref. 21) are unaffected by suction in either region and resemble profiles for the two-dimensional boundary-layer flows as expected. At station 3 (not shown), a perceptible drop in pitot pressure because of bleed is evident at about $y/\delta = 0.1$ for region I bleed (case D) in contrast to region II bleed (case E), which shows negligible influence at this station. Similarly, region I bleed displays reduced yaw angles up to about $y/\delta_\infty = 0.8$ whereas region II bleed has no significant effect. This general behavior is also seen at stations 4 (not shown) and 5 (Fig. 12), both of which lie upstream of region II. In Fig. 12, the ordinate (y/δ) is the distance normal to the flat plate, and the abscissa is the pitot pressure (Fig. 12a), normalized by the freestream pitot pressure, or yaw angle in degrees (Fig. 12b). Although region II bleed has no influence at either of these stations, region I bleed exhibits a "cross-over" point, i.e., near the flat plate (up to about $y/\delta_\infty = 0.7$ for station 5) the pitot pressure increases above its no-bleed value, whereas at larger distances from the plate the pitot pressure is slightly lower. The overshoot at $y/\delta \sim 1.0$ is associated with the compression fan near the plate. This overshoot is reduced with region I bleed and is reflected in a tightening of the upstream leg of the compression fan. A similar observation was previously made regarding the weaker interaction (case B). The yaw angles at both stations (4 and 5) are lower for region I bleed with no effect of region II bleed. At station 8 (Fig. 13), the pitot pressure for region II bleed is higher very close to the flat plate, accentuating the s-shaped structure observed in previous research.[7] In the major portion of the boundary layer, however, the pitot pressure closely parallels the no-bleed profile. Yaw angles for region II bleed show no significant deviation from no-bleed (case C) values.

The computed wall pressure is compared with the experimental data of Goodwin[25] in Fig. 14 at the spanwise location $z/\delta = 5$. The ordinate is the static pressure normalized by the

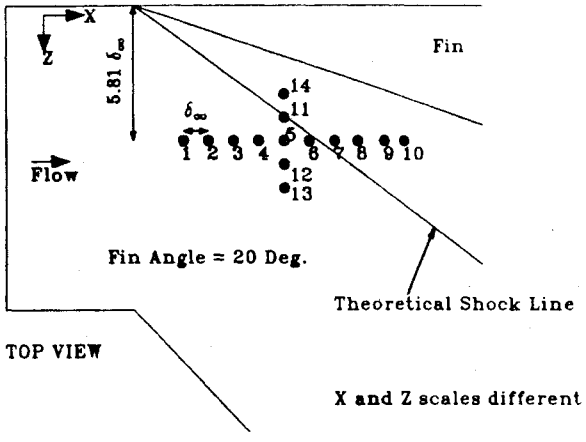

Fig. 11 Experimental locations of Shapey and Bogdonoff (20-deg SFC).

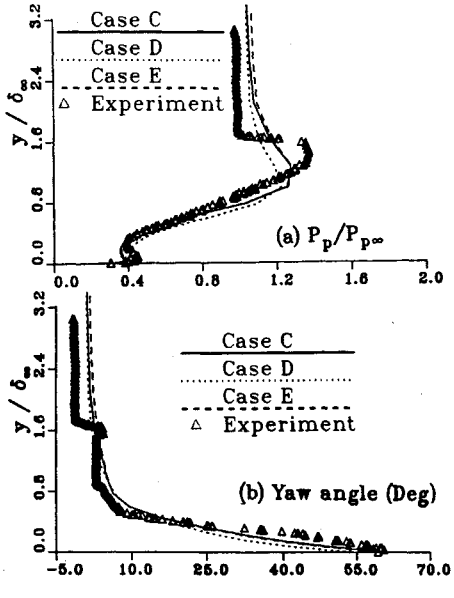

Fig. 12 Pitot pressure and yaw angles, station 5 (20-deg SFC).

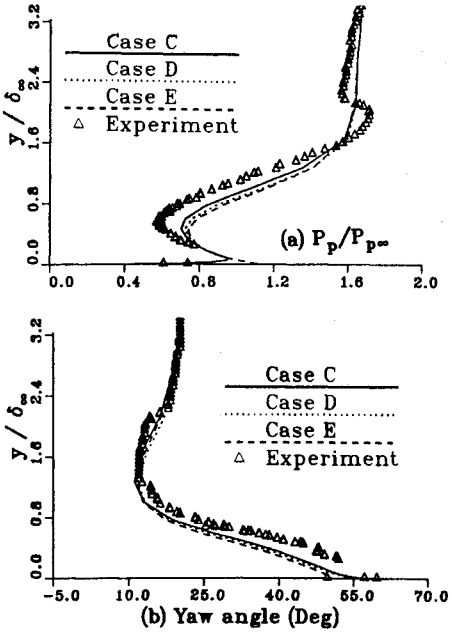

Fig. 13 Pitot pressure and yaw angles, station 8 (20-deg SFC).

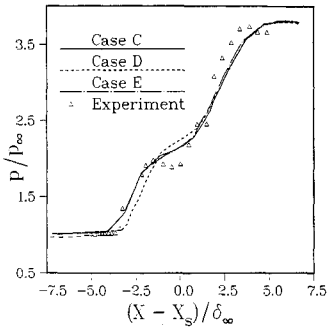

Fig. 14 Surface pressure, $z/\delta = 5$ (20-deg SFC).

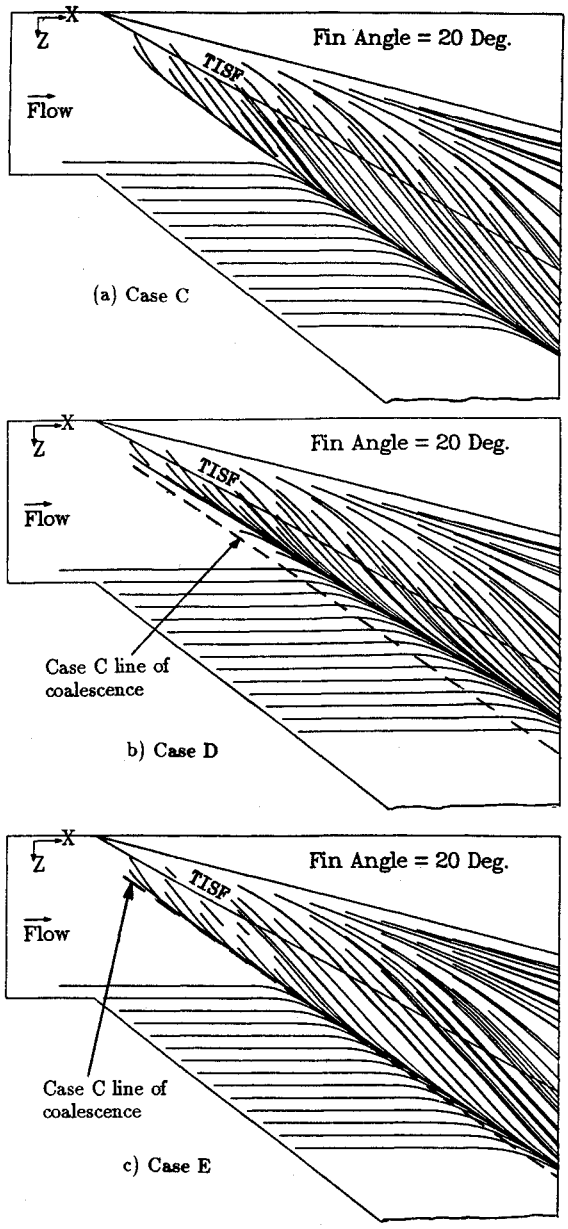

Fig. 15 Surface streamlines (20-deg SFC).

freestream static pressure. The abscissa is the streamwise distance (measured relative to the inviscid shock) normalized with δ_∞. Comparison of case C with experimental data indicates good agreement with regard to upstream influence. The experimental data indicate a plateau region at about $(x - x_s \sim 0)$ that is not adequately reproduced in the computation, perhaps for lack of grid resolution. The total pressure rise equals the expected theoretical value in the inviscid region and is independent of bleed region and magnitude. The effect of region I bleed (case D) is evidently to reduce upstream influence, thus reducing modestly the distance over which the pressure rise is achieved. Region II bleed (case E) does not affect the upstream influence or the total pressure rise.

Several of the observations made previously for the weaker interaction may be repeated. Local skin friction values show steep increases only in the bleed regions but are not affected elsewhere. Eddy viscosity values are reduced in the boundary layer directly above the bleed region. The size of the upstream compression fan is reduced by region I bleed. Region II bleed however has no effect on either leg of the compression fan. There is no effect of bleed on the flow variables beyond $y/\delta \sim 2.5$.

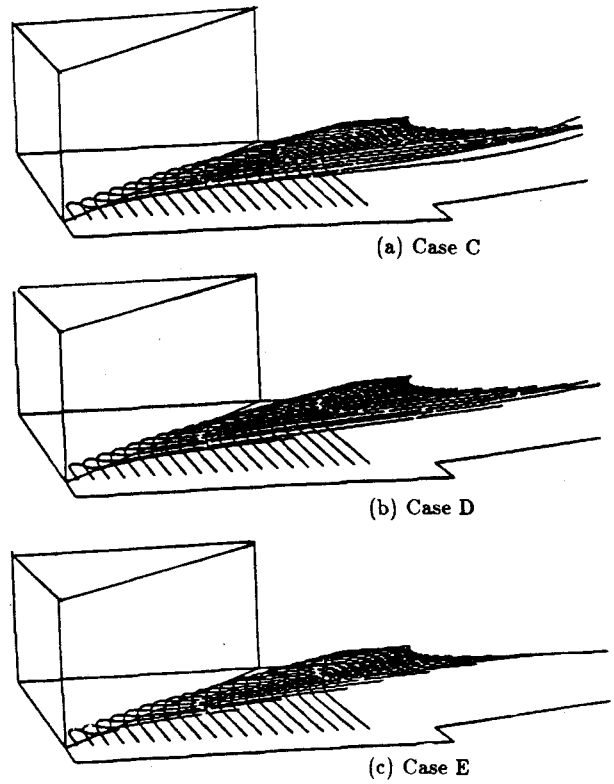

Fig. 16 Particle traces, $y/\delta = 0.6$ (20-deg FSC).

Effect of Suction on Flowfield Structure

The computed solutions are utilized to examine the effect of bleed on the flow structure. Figure 15 displays surface streamlines for cases C, D, and E, respectively. The location of the inviscid shock is indicated in each figure. The line of coalescence clearly persists for all cases. Whereas region I suction (Fig. 15b) tends to align the line of coalescence with the theoretical inviscid shock footprint, region II suction (Fig. 15b) has no significant influence despite the previously discussed steep local increase in skin friction values downstream of the TISF. This is another manifestation of the conclusion derived from the surface pressure plot, viz., region I bleed reduces upstream influence whereas region II bleed has no such effect.

Further analysis of the computed flowfield is carried out with three-dimensional particle traces. Traces of particles released at $y/\delta_\infty = 0.0001$ (not shown) indicate that for case C, these particles coalesce to form the line of coalescence observed in the surface streamlines. For case D, the particles are ingested by the plate in the region of bleed, whereas particles for case E follow trajectories similar to those for case C. Figure 16 shows traces of particles released at $y/\delta_\infty = 0.6$. For both cases C and D, the particles are entrained in the vortical structure. For case E, those particles originating near the leading edge of the fin at the upstream boundary (small values of the spanwise coordinate z) are ingested by the flat plate in region II—note the trajectories of the first seven particles from the fin leading edge. The other particles are swept into the vortical structure as for cases C and D. It is evident that only those particles whose no-bleed trajectory passes close to the flat plate (to within a certain height whose spatial variation is difficult to estimate) are ingested. These figures show clearly that the mean flowfield pattern continues to be dominated by the vortical structure for both bleed regions.

A few observations about cases F and G are in order. The general effect of increasing bleed in region I is monotonic in the sense that the same observations made for case D are valid only to a greater extent. The pitot pressure overshoot, shown for case D in Fig. 12, for example, is further reduced, and in fact, for case G this overshoot disappears entirely. The tight-

ening of the upstream compression fan is also enhanced. The line of coalescence (Fig. 15b) moves further downstream toward the line representing by choice both the shock trace and the downstream boundary of the bleed region. Particle traces indicate that despite the fact that a larger portion of the boundary layer is ingested, the large vortical structure is retained.

VII. Conclusions

The effect of suction on the supersonic flow past the single fin configuration is investigated. Two fin angles—8 deg and 20 deg—are considered, both at Mach 3. The former is an incipiently separated configuration for which experimental data incorporating suction are available. The latter represents a strong interaction for which the existence of the vortical structure has been previously demonstrated. For the 8-deg fin, the area of suction considered is roughly rectangular and covers a strip on either side of the theoretical shock foot print. For the 20-deg fin, bleed is applied on two regions on the plate jointly spanning the region between the line of upstream influence and the base of the fin.

For both interaction strengths, surface turning angles are generally reduced in the presence of bleed. Local skin friction values, on the other hand, display steep increase in the bleed region. For the stronger interaction, the line of coalescence persists for all suction magnitudes and areas considered. Since the weaker interaction does not display a clear line of coalescence in the absence of bleed, an equivalent statement cannot be made. Detailed examination of the flow past the 20-deg fin indicates that the width of the upstream compression fan formed by the shock wave near the plate is significantly reduced with region I bleed, for which upstream influence is also reduced and the rate of pressure rise on the plate is higher, although the total pressure rise remains roughly the same. Suction aft of the shock (region II) does not produce any substantial change in flow structure. The vortical structure persists for both bleed regions, indicating that such high Reynolds number turbulent interactions are robust and cannot be easily manipulated by suction. The effect of suction is to ingest particles whose no-bleed trajectory falls in the close vicinity of the bleed area without affecting the overall flowfield in any significant fashion. This may have some implication for the control of turbulent interactions in high-speed propulsion inlets.

Acknowledgments

This research was sponsored by the Air Force Office of Scientific Research under AF Grant 86-0266 monitored by J. McMichael and L. Sakell. The authors would like to thank C. C. Horstman and S. Bogdonoff for many helpful discussions. The computations described were performed at the NASA Research Centers at Ames and Langley. The assistance of the staff at both centers is gratefully acknowledged.

References

[1]Inger, G., "Supersonic Viscous-Inviscid Interaction of a Swept Ramp with a Turbulent Boundary Layer," AIAA Paper 85-1669, July 1985.

[2]Stalker, R., "Spanwise Propagation of Disturbances in Swept Shock Wave-Boundary Layer Interactions," AIAA Paper 82-0988, June 1982.

[3]Stanbrook, A., "An Experimental Study of the Glancing Interaction Between a Shock Wave and a Boundary Layer," British Aeronautical Research Council, ARC CP-555, Bedford, England, UK, July 1960.

[4]Kubota, H., and Stollery, J., "An Experimental Study of the Interaction Between a Glancing Shock Wave and a Turbulent Boundary Layer," *Journal of Fluid Mechanics,* Vol. 116, March 1982, pp. 431-458.

[5]Oskam, B., Vas, I., and Bogdonoff, S., "An Experimental Study of 3-D Flowfields in an Axial Corner at Mach 3," AIAA Paper 77-689, June 1977.

[6]Horstman, C., and Hung, C., "Computation of Three-Dimensional Turbulent Separated Flows at Supersonic Speeds," AIAA Paper 79-0002, Jan. 1979.

[7]Knight, D., Horstman, C., Shapey, B., and Bogdonoff, S., "Structure of a Supersonic Turbulent Flow Past a Sharp Fin," *AIAA Journal,* Vol. 25, No. 10, 1987, pp. 1331-1337.

[8]Knight, D., Horstman, C., Ruderich, R., Mao, M-F., and Bogdonoff, S., "Supersonic Turbulent Flow Past a 3-D Swept Compression Corner at Mach 3," AIAA Paper 87-0551, Jan. 1987.

[9]Knight, D., Raufer, D., Horstman, C., Ketchum, A., and Bogdonoff, S., "Supersonic Turbulent Flow Past a Swept Compression Corner," AIAA Paper 88-0310, Jan. 1988.

[10]Token, K., "Heat Transfer Due to Shock Wave/Turbulent Boundary Layer Interactions in High Speed Weapons Systems," Air Force Flight Dynamics Laboratory, AFFDL-TR-74-77, Wright-Patterson Air Force Base, OH, 1974.

[11]Settles, G., and Dolling, D., "Swept Shock Wave Boundary-Layer Interactions," *Tactical Missile Aerodynamics,* Progress in Astronautics and Aeronautics Series, Vol. 104, AIAA, New York, 1986, pp. 297-379.

[12]Mee, D., and Stalker, R., "Investigation of Weak Shock-Shock and Shock-Expansion Intersection in the Presence of a Turbulent Boundary Layer," AIAA Paper 87-0549, Jan. 1987.

[13]Batcho, P., Ketchum, A., Bogdonoff, S., and Fernando, E., "Preliminary Study of the Interactions Caused by Crossing Shock Waves and a Turbulent Boundary Layer," AIAA Paper 89-0359, Jan. 1989.

[14]Barnhart, P., Greber, I., and Hingst, W., "Glancing Shock Wave-Turbulent Boundary Layer Interaction with Boundary Layer Suction," AIAA Paper 88-0308, Jan. 1988.

[15]Knight, D., "A Vectorized Three-Dimensional Navier-Stokes Code for High Speed Inlets," Rutgers University, New Brunswick, NJ, RU-TR-161-MAE-F, March 1984.

[16]Baldwin, B., and Lomax, H., "Thin Layer Approximation and Algebraic Model for Separated Flows," AIAA Paper 78-257, Jan. 1978.

[17]Buleev, N., "Theoretical Model of the Mechanism of Turbulent Exchange in Fluid Flows," Atomic Energy Research Establishment, TR 957, Hartnell, England, UK, 1963.

[18]Cebeci, T., and Smith, A., *Analysis of Turbulent Boundary Layers,* Academic, New York, 1974.

[19]Gaitonde, D., and Knight, D., "Numerical Experiments on the 3-D Shock Wave-Boundary Layer Interaction Generated by a Sharp Fin," AIAA Paper 88-0309, Jan. 1988.

[20]York, B., "Evaluation of the Baldwin-Lomax Turbulence Model for a Class of Boundary Layer Flows," M.S. Thesis, Dept. of Mechanical and Aerospace Engineering, Rutgers Univ., Piscataway, NJ, 1984.

[21]Gaitonde, D., "Numerical Investigation of Some Control Methods for 3-D Turbulent Interactions Due to Sharp Fins," Ph.D. Dissertation, Dept. of Mechanical and Aerospace Engineering, Rutgers Univ., Piscataway, NJ, 1989.

[22]Knight, D., "A Hybrid Explicit-Implicit Numerical Algorithm for the Three-Dimensional Compressible Navier-Stokes Equations," *AIAA Journal,* Vol. 22, No. 8, 1984, pp. 1056-1063.

[23]Gaitonde, D., and Knight, D., "Numerical Investigation of Some Control Methods for Turbulent Interactions Due to Sharp Fins," AIAA Paper 89-0360, Jan. 1989.

[24]McClure, W., and Dolling, D., "Flowfield Scaling in Sharp Fin-Induced Shock Wave/Turbulent Boundary Layer Interactions," AIAA Paper 83-1754, July 1983.

[25]Goodwin, S., "An Exploratory Investigation of Sharp-Fin Induced Shock Wave/Turbulent Boundary Layer Interactions at High Strengths," M.S. Thesis, Dept. of Aerospace and Mechanical Engineering, Princeton Univ., Princeton, NJ, 1984.